arXiv:astro-ph/0202182v1 8 Feb 2002

OH–SELECTED AGB AND POST–AGB OBJECTS.
I. INFRARED AND MASER PROPERTIES

Maartje N. Sevenster[1]

MSSSO/RSAA, Cotter Road, Weston ACT 2611, Australia

Draft version February 1, 2008

ABSTRACT

Using 766 compact objects found in a systematic survey of the galactic Plane in the 1612–MHz masing OH line, new light is cast on the infrared properties of evolved stars on the thermally–pulsing asymptotic giant branch and beyond. The usual mid–infrared selection criteria for post–AGB, based on IRAS colours, largely fail to distinguish early post–AGB stages. A two–colour diagram from much narrower–band MSX flux densities, with bimodal distributions, provides a better tool to do the latter. Four mutually consistent selection criteria for OH–masing red proto–planetary nebulae are given, as well as two for early post–AGB masers and one for all post–AGB masers including the earliest ones. All these criteria miss a group of blue, high–outflow post–AGB sources with 60–μm excess; these will be discussed in detail in Paper II. The majority of post–AGB sources show regular double–peaked spectra in the OH 1612–MHz line, with fairly low outflow velocities, although the fractions of single peaks and irregular spectra may vary with age and mass. The OH flux density shows a fairly regular relation with the stellar flux and the envelope optical depth, with the maser efficiency increasing with IRAS colour R_{21}. The OH flux density is linearly correlated with the 60–μm flux density.

Subject headings: Stars:AGB and post-AGB

1. INTRODUCTION

Maser emission in the satellite line of groundstate OH at 1612.231 MHz occurs in a variety of stellar objects. Star–forming regions (SFR), super giants, visible (Miras) and invisible (OH/IR) oxygen–rich stars at the tip of the asymptotic giant branch (AGB) and post–AGB transition objects or even young planetary nebulae can all show maser emission at 1612 MHz. Spectral shapes and variability are thought to differ for the different types of object (see eg. te Lintel Hekkert & Chapman 1996).

Objects are often selected as AGB or post–AGB candidates by the two colours from their flux densities at 12 μm, 25 μm and 60 μm measured by IRAS (InfraRed Astronomical Satellite). (eg. te Lintel Hekkert et al. 1991; Lewis 1994 and references therein). In the resulting two–colour diagram, a "main sequence" for oxygen–rich AGB stars can be identified, where the location of an object is determined by its age, initial mass and possibly metallicity (see eg. Bedijn 1987; Likkel 1989). This sequence is called the "evolutionary" sequence (van der Veen & Habing 1988). To test the usual selections, especially of post–AGB objects, and potentially find less ambiguous criteria, in this paper the approach is, for the first time, from an OH–selected sample, finding its IR properties, rather than finding the OH properties of an IR–selected sample. Moreover, IRAS colours are combined with colours at shorter infrared wavelengths from the Midcourse Space Experiment (MSX) and 2–Micron All Sky Survey (2MASS).

The sample consists of 766 compact, OH–masing sources[2] in the galactic Plane (for all details see Sevenster et al. 1997a,1997b,2001). The IRAS (12,25,60,100 μm), MSX (4,8,12,15,21 μm) and 2MASS identifications (J,H,K) were taken from the respective public databases.

Matches were found for 587 (IRAS, within 3σ error ellipse), 494 (MSX, within 5″) and 194 (2MASS, within 3″) objects, respectively. Note that the 2MASS mission has not yet covered the entire section of the plane covered by the OH sample. For many sources that do have a valid positional identification, several or most of the flux densities may not have been measured properly. For instance, out of the 587 IRAS identifications, only 240 have well–determined 12–μm , 25–μm ánd 60–μm flux densities (quality flag 2 or 3). The relatively small percentage of IRAS identifications is caused largely by the confusion at the very low latitudes of our survey ($|b| < 3°.25$). For the same reason, the flux–density measurements, especially at 60 μm and 100 μm, are likely to be somewhat overestimated even if they are not flagged as "upper limits" in the IRAS data base. With the exception of a few likely supergiants, none of the sources could be identified with an optical counterpart. The combination of low latitude and OH–based selection means that lowest–mass AGB stars ($< 1\,\mathrm{M_\odot}$) may be underrepresented in the sample.

The aim of this analysis is to find generic differences between post–AGB and AGB objects, both in infrared and maser properties, and signs of post–AGB evolution. We will define a post–AGB stage as the phase after the last thermal pulse, when variability has ceased. The term proto–planetary nebula (PPN) will indicate a slightly later stage, when the mass–loss rate has dropped by orders of magnitude and the near–infrared or even optical emission is becoming much stronger with respect to the mid–infrared. Sometimes such objects are called OHPN, as they may already show radio continuum (PN), but still harbour masers (OH). However, as long as an object shows OH–maser emission, especially at 1612 MHz as our sample

---

[1]sevenste@strw.leidenuniv.nl

[2]A self–explanatory archive of all OH and IR data for all objects can be downloaded from http://www.mso.anu.edu/~msevenst
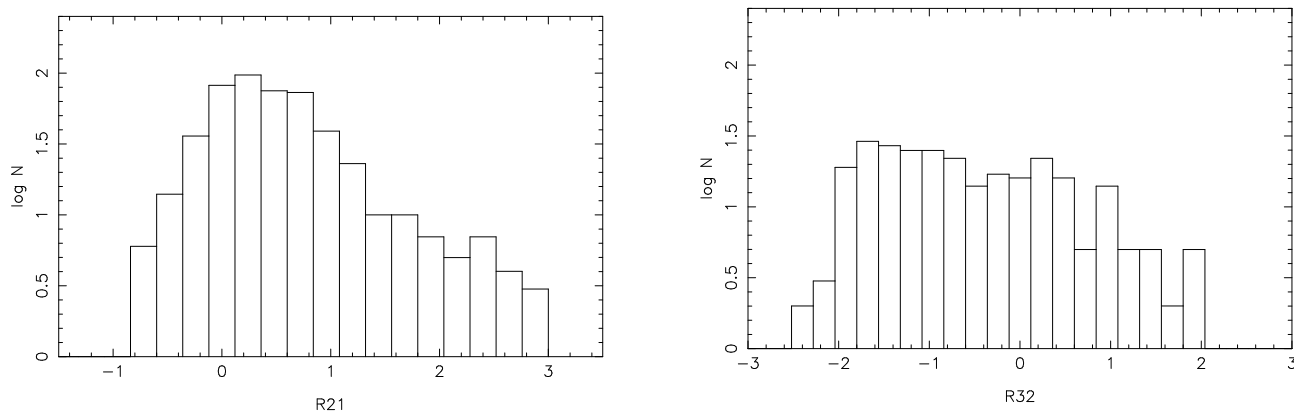
1

FIG. 1.— The histograms of the two main IRAS colours ($R_{21} = [12 - 25]$ and $R_{32} = [25 - 60]$) for all OH–selected sources with well–determined flux–density measurements for all three bands involved.

does, it is per definition not a full–blown PN (Zijlstra et al. 1989; Lewis 1989).

In Section 2, we will introduce an MSX two–colour diagram. In Section 3, we discuss the role of the OH outflow velocity and the spectral shapes of different types of objects and in Section 4 the near–infrared properties are added to the discussion. In Section 5 some selection criteria for late– versus early post–AGB objects are summarized and evidence from known sources presented, then in Section 6 a new expression for OH 1612–MHz maser efficiency in (post–) AGB objects is given. Conclusions are presented in Section 7.

2. DISTRIBUTIONS OF MID–INFRARED COLOURS

All mid–infrared (MIR) colours are defined as $[a - b] = 2.5 \log(S_b/S_a)$ with S flux density in Jy and a,b wavelength in μm. For IRAS, the usual names $R_{21} \equiv [12 - 25]$ and $R_{32} \equiv [25 - 60]$ are used, as well as $R_{43} \equiv [60 - 100]$. The 12–μm bands of the two satellites are different : for MSX it covers 11.1 μm to 13.2 μm, for IRAS 8.5 μm to 15.5 μm. This means, most importantly, that the 9.7–μm silicate feature is in the MSX 8–μm band (6.8 μm to 10.8 μm) whereas it is in the IRAS 12–μm band. Only in very cold material may the silicate feature shift into the MSX 12–μm band (Zhang & Kwok 1990). The MSX 15–μm band is almost entirely included in the IRAS 12–μm band and similarly the MSX 21–μm band is almost entirely included in the IRAS 25–μm band.

In Fig. 1&2, histograms are shown for five MIR colours. The distributions for $[8 - 12]$ and $[15 - 21]$ immediately stand out as curiously bimodal when compared to the other three, with divisions at $\sim$0.9 and $\sim$0.7, respectively. To follow this up, we use those two colours for the MSX two–colour diagram. All sources with these MSX colours well–defined are plotted in Fig. 3. The bulk of the sources is in the bluest quadrant, with little spread in colour, but a second group is at much redder $[8 - 12]$ with a large spread in $[15 - 21]$.

In Fig. 4, the traditional IRAS colour–colour diagram is shown, with the evolutionary sequence and the regions as laid out by van der Veen & Habing (1988) and symbols defined by MSX colour. The circles are found in the region where one typically expects late post–AGB objects by IRAS colours (region V and further; Bedijn 1987; van der Veen & Habing 1988 ("non–variable OH/IR stars")).

The bulk of the main MSX group is along the evolutionary sequence, except for a surprisingly large group in the left part of region VIII and above. The crosses are found mostly straddling the border between V and VIII, below the "bipolar outflow" region, defined recently by Zijlstra et al. (2001). A solitary '+' is right on the edge of where one expects to find OH–emitting SFRs (Braz & Sivagnanam 1987); in this region there is strong overlap between PPN and SFRs.

The bimodality of the two MSX–colour distributions suggests the existence of at least two intrinsically different types of objects in the sample. Combining this with what one already understands from the traditional IRAS colour–colour diagram (van der Veen & Habing 1988), it seems that the transition from blue ($<$0.9) to red ($>$0.9) $[8 - 12]$ coincides with the transition off the AGB. The transition from blue ($<$0.7) to red ($>$0.7) $[15 - 21]$ could well indicate a next evolutionary transition, further away from the evolutionary sequence (Fig. 4), such as the drop in mass–loss rate and start of the fast PPN wind (cf. van Hoof et al. 1997). Hence, the MSX diagram possibly distinguishes between different post–AGB stages and provides an easier tool to separate post–AGB stars from AGB stars, but does not distinguish between different AGB objects like the IRAS diagram with its evolutionary sequence. The two diagrams should be used in combination.

3. THE ROLE OF THE OH–SHELL OUTFLOW VELOCITY

The outflow velocity $V_{\exp}$ of a typical OH maser spectrum is thought to be related to the luminosity (age, initial mass) and the metallicity (age, galactic coordinates) of the central star, via

$$L_* = V_{\exp}^4 Z^{-2} \qquad (1)$$

according to van der Veen (1989; see also Habing et al. 1994). Not all OH maser spectra are regular and double–peaked, so the outflow velocity is not always well-defined. Specifically, some suspected post–AGB objects may have spectra ranging over almost 100 km s^{-1} (e.g. spectrum 2 in Fig. A7; see also te Lintel Hekkert & Chapman 1996), but be listed as single–peaked with just the peak velocity, whereas similar objects do have an associated outflow velocity (Fig. A1(4$^{\text{th}}$–last)). Such single–peaked objects are intrinsically different from star-forming regions, that commonly – especially with sufficient spatial
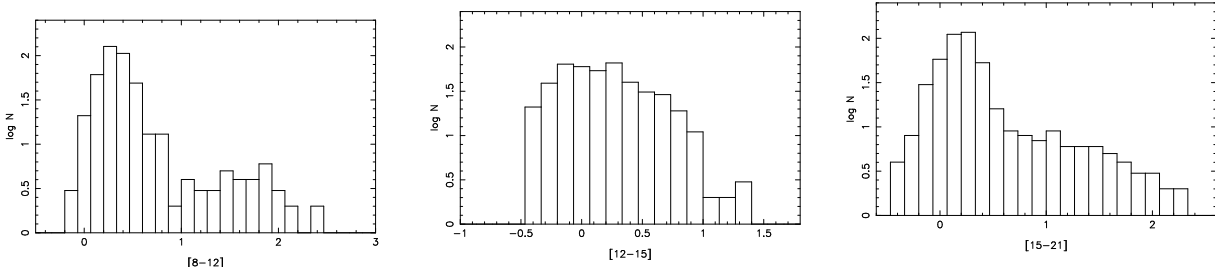
FIG. 2.— The histograms for the three main MSX colours, for all sources with well–determined flux densities in both bands of each colour. The $[8-12]$ and $[15-21]$ distributions look very different from the $[12-15]$ distribution, as well as from the distributions in Fig. 1, and seem bimodal with minima around 0.9 and 0.7, respectively.
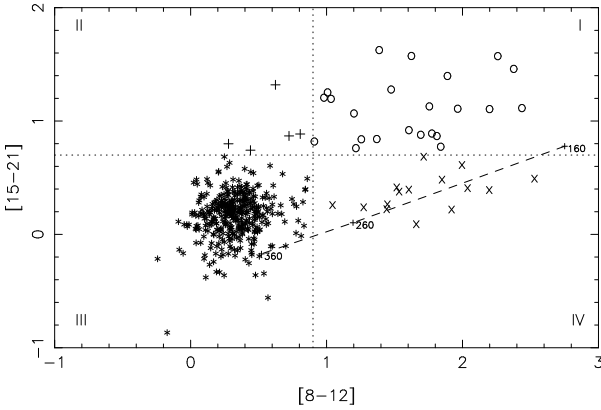

FIG. 3.— A two–colour diagram for MSX colours, split into four quadrants according to the apparent minima in the bimodal distributions shown in Fig. 2. Objects are plotted with different symbols accordingly (circles in the first quadrant, plusses in the second, etc.), that will be used to relate their locations in other diagrams to their MSX colours. The dashed line shows the colours for black–body radiation at various temperatures (tags).
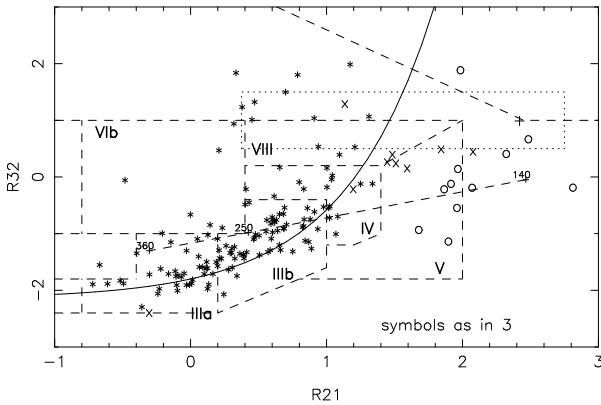

FIG. 4.— The two–colour diagram for IRAS colours, with symbols as defined by the quadrants in Fig. 3. The solid curve indicates the evolutionary sequence and the dashed boxes the regions as defined by van der Veen & Habing (1988). The dashed line separates roughly the red corner of OH–emitting SFRs (Braz & Sivagnanam 1987; see Section 5.3). (Non–OH–emitting SFRs would be found to the left of this region at $R_{32} > 2$.) The dotted rectangle is the region classified as "bipolar outflow" region by Zijlstra et al. (2001). Note that compared to Fig. 3 there are far fewer objects, as now the IRAS colours, as well as the MSX colours, have to be well–defined as well as the MSX colours.
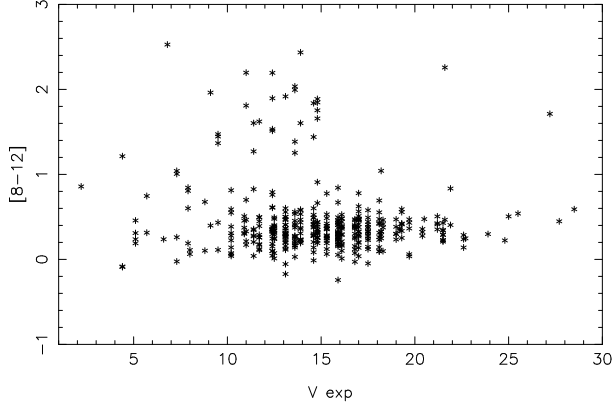
FIG. 5.— The MSX $[8-12]$ colour plotted against OH outflow velocity. The general group of AGB sources with $[8-12] \sim 0.4$ ranges over all outflow velocities. There is a discrete group of sources with much redder colour, indicating they are post–AGB and PPN sources. Their outflow velocities are limited to the range 9–15 km s^{-1}. The same trend is seen – less clearly – for R_{21} and $[15-21]$, but not for any of the other IR colours.
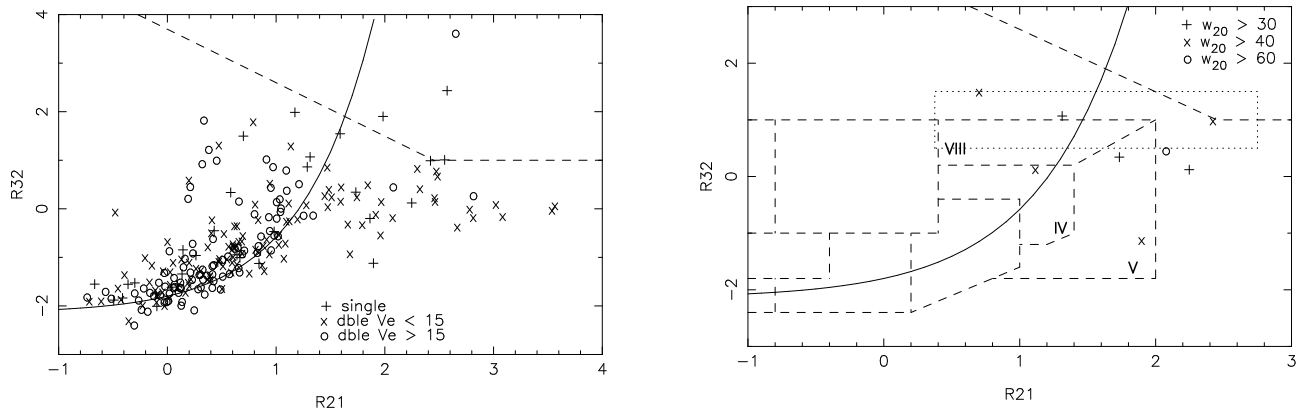

FIG. 6.— As Fig. 4, with symbols according to outflow velocity. The extremely red single–peaked sources ('+') in the top panel are most likely to be SFRs. The PPN region is populated mostly by sources with outflow velocities below 15 km s^{-1} (as derives from Fig. 4&5). Interesting is the region to the left of the evolutionary sequence, with $0 < R_{32} < 2$, where sources have mostly outflow velocities *higher* than 15 km s^{-1}. Before (Fig. 3& 4), these sources were found to have very blue MSX colours. Irregular sources (Section 3) are found in and around the bipolar–outflow region (lower panel). The spectra of the irregular sources are shown in Fig. A7.

resolution – have just one very narrow bright peak in their 1612–MHz spectrum, single–peaked PN (Fig. A1(13)) or single–detected AGB stars, that simply have one of the peaks missing due to detection limits (cf. Fig. A1(15)). Hence, selecting V_{exp}=0 km s^{-1} results in a hotchpotch of objects.

We want to find out what OH outflow velocity and spectral "shape" tell us about the evolutionary stage of an object. In Fig. 5, $[8-12]$ is plotted against outflow velocity. A population of red sources is clearly separated from the rest, with outflow velocities between 9 km s^{-1} and 15 km s^{-1}. The separation is at $[8-12] \sim 0.9$, as before (Fig. 2&3); for $[15-21]$ a similar but less clear separation is found at ~ 0.7. Thus, interestingly, in the first and fourth quadrant of Fig. 3, all double–peaked sources are found to be in this very limited range of outflow velocities.

In the IRAS colour–colour diagram (Fig. 6a), region V and beyond is populated mainly by lower–outflow velocity objects, as follows from the previous two figures. The single–peaked sources in the reddest corner of this diagram are most likely SFRs. On the evolutionary sequence, the spread in outflow velocities is largest. We do not find the increase of outflow velocity with R_{21} for blue sources that is reported in Chen et al. (2001), but our OH–selected sample is probably too red to see this. The higher outflow velocities prevail in the left–hand sides of regions IV and VIII, where we noted relatively high numbers of sources before (Section 2). These sources may also be post–AGB sources (van der Veen & Habing 1988); they will be discussed in Paper II (Sevenster 2002).

Post–AGB stars, typically selected from region V, are often connected to irregular, extreme–velocity outflows (te Lintel Hekkert & Chapman 1996). However, looking at the OH spectra for these sources (Fig. A1), they correspond to OH–selected sources with mostly normal, double–peaked, intermediate–outflow spectra (Table 1). The same is true for the higher–outflow sources to the left of the evolutionary sequence, although the fraction of irregular spectra is higher (Fig. A5, Table 1).

This is not to say that there is no subset of irregular sources with reasonably confined properties. In Fig. A7, the spectra are shown for all sources from the full sample that have velocity widths (w_{20}) much larger than the peak separation ($\Delta V \equiv 2V_{exp}$). This criterion is used as an indicator of non–spherical, irregular outflow. Their IRAS colours (Fig. 6b) clearly indicate a connection to the bipolar–outflow region of Zijlstra et al. (2001). The actual velocity widths are up to 70 km s^{-1}.

In summary, although very irregular OH spectra may always indicate a post–AGB host, the reverse may not be true. Unless the strong reddening in $[8-12]$ and R_{21} is unrelated to the onset of post–AGB processes, OH 1612–MHz spectra of post–AGB objects seem to be mainly regular and show no indication of irregular mass loss or increased outflow velocity, spherical nor bipolar. For the bulk of the red post–AGB objects, the outflow velocities are even lower than average: between 9 km s^{-1} and 15 km s^{-1}. Most likely, this indicates that the OH masers in general disappear before the changes of the central wind truly influence the envelope at such large radii.

4. NEAR–INFRARED PROPERTIES

From the 2MASS database, J (1.25 μm), H (1.65 μm) and/or K (2.17 μm) magnitudes were obtained for 194 sources. Colours are used as uncorrected J–H and H–K. The two–colour diagram is shown in Fig. 7. Using the symbols from Fig. 3, post–AGB stars are where one may expect them (e.g. Garcia–Lario et al. 1997) but the diagram can hardly be used as a diagnostic for any particular type of object (see also Fig. 10c).

An alternative to the IRAS colour–colour diagram was proposed by van Hoof et al. (1997), using $[12] - [25]$ and K–$[12]$ (Fig. 8), with IRAS magnitudes $[12] \equiv 2.5 \log(59.5/S_{12})$ and $[25] \equiv 2.5 \log(13.4/S_{25})$ following Oudmaijer et al. (1992). The PPN symbols from Fig. 3 (circles) are exclusively at $[12] - [25] \gtrsim 3.5$. In the bottom panel the selection is based on OH properties, as well as $[15-21]$. The latter colour is used for the selection, rather than $[8-12]$, because it may single out the further–evolved post–AGB sources (i.e. PPNe). Selecting V_{exp} between 9 km s^{-1} and 15 km s^{-1} (Fig. 5) and the sum of the OH flux densities of the two peaks larger than 1 Jy, we find a sample (circles) that occupies the same region as the circles in Fig. 8(a). The dashed line in these diagrams is drawn to separate the circles from the other objects.

The post–AGB selection of Fig. 8(b), based largely on OH spectral properties, gives *without further assumptions* $[12] - [25] > 3$ and K–$[12] < 9$, as well as $[8-12] > 0.9$. This once more confirms that the sources in the first quadrant of Fig. 3 are "standard" post–AGB sources, moving to higher R_{21} in the IRAS two–colour diagram (Bedijn 1987; van der Veen & Habing 1988), and that these are mostly regular and double–peaked (Fig. A3). A second mixed near–mid–infrared two–colour diagram is shown in Fig. 9. The red post–AGB group separates clearly from the main oxygen–rich colour sequence (see van Loon et al. (1998)). However, some objects that are still in the third quadrant of the MSX diagram – and on the IRAS evolutionary sequence – are also above the dashed curve and quite distinctly separated from the main colour sequence. This may indicate that they are in the very first stages of post–AGB colour change.

In conclusion, the NIR magnitudes of objects are useful to distinguish (post–) AGB evolutionary stages primarily in combination with the 12–μm and 25–μm IRAS flux densities.

5. OH SPECTRA OF IR SELECTED SOURCES

5.1. *Selecting post–AGB sources*

Summarizing the previous three sections, standard "cold" evolved OH PPN objects can thus be selected virtually consistently in four ways.

- (1) The traditional IRAS selection : $R_{32} \lesssim 1.5$ and $R_{21} \gtrsim 1.4$ (Fig. 4). Spectra are shown in Fig. A1.

- (2) From MSX colours : $[8-12] > 0.9$ and $[15-21] > 0.7$ (Fig. 3). Spectra are shown in Fig. A2.

- (3) From OH 1612–MHz properties : $V_{exp} = 12 \pm 3$ km s^{-1} and $S_{OH,blue} + S_{OH,red} > 1$ Jy (resolution ~ 2 km s^{-1}), with $[15-21] > 0.7$ (Fig. 8b). Spectra are shown in Fig. A3.

- (4) With NIR : $[12] - [25] > 4.164 - 0.164$ (K $-[12]$) and K$-[12] < 9$ (Fig. 8a). This selection is mostly a
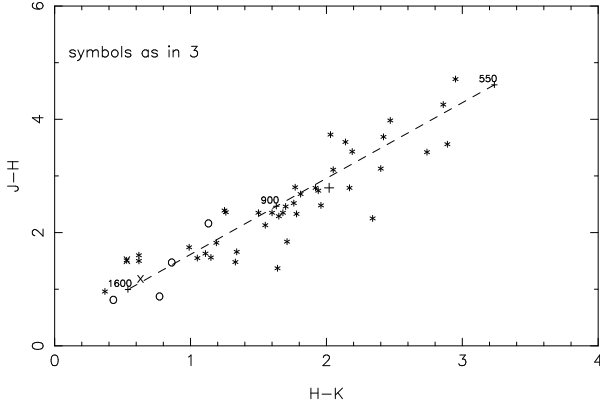
FIG. 7.— The 2MASS two–colour diagram (Section 4) with symbols defined by MSX colours (Fig. 3). The dashed line connects black–body colours for several temperatures. For J−H < 0.4, Garcia–Lario et al. (1997) find exclusively planetary nebulae (PNe can be found at redder colours). None of our OH–masing sources are that blue, which would agree with the idea that masers, especially the 1612–MHz OH maser, cannot exist in the environment of a truely ionized, high–wind nebula.
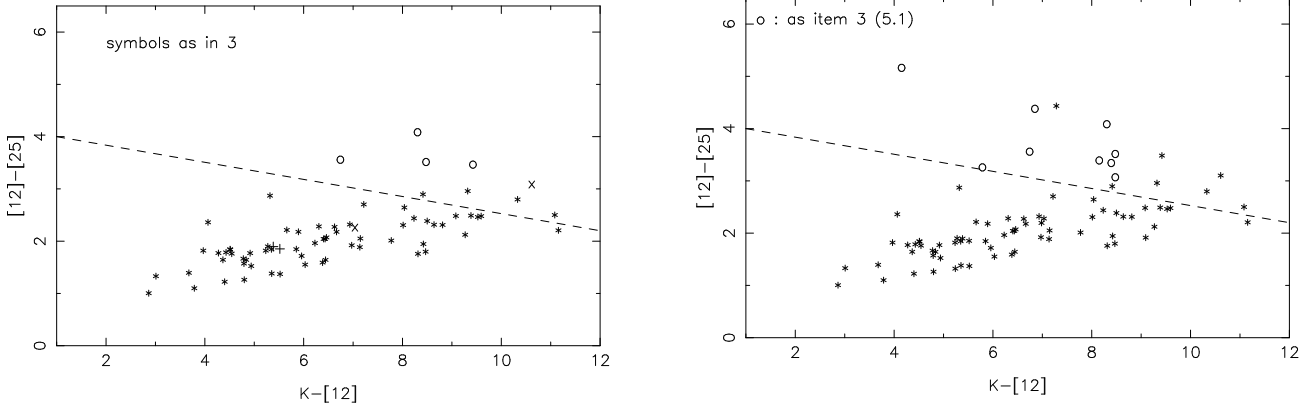

FIG. 8.— The two–colour diagram using combined MIR and NIR colours as defined in Section 4, following van Hoof et al. (1997). **a.** Symbols defined by MSX colour (Fig. 3). **b.** Symbols defined mainly by OH properties. The circles indicate sources with outflow velocities between $9\,\mathrm{km\,s^{-1}}$ and $15\,\mathrm{km\,s^{-1}}$, the sum of the two peak–flux densities larger than 1 Jy and [15 − 21]>0.7. They also have [15 − 21] > 0.7. Based on our previous findings, these sources are likely "standard" PPN sources. Note that all circles have K−[12] < 9, which is relevant in the context of Fig. 10.
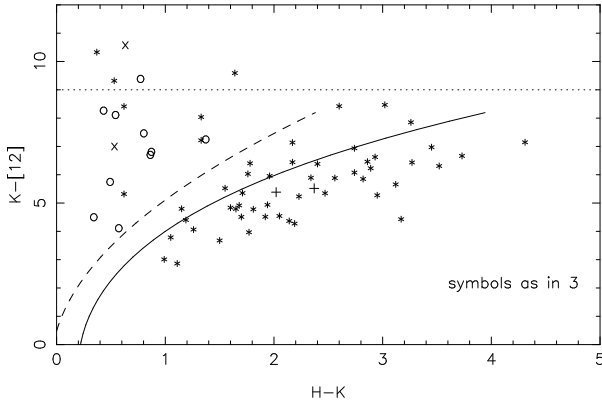

FIG. 9.— The two–colour diagram using combined MIR and NIR colours as defined in Section 4, following van Loon et al. (1998). The solid curve indicates their oxygen–rich AGB sequence; the dashed curve is our separation between AGB and post–AGB objects. The post–AGB sources, from quadrants I and IV (Fig. 3), are all found above this line. Quite a few sources from quadrant III are found in the post–AGB region, however, which suggest that this diagram might provide a tool to distinguish the earliest post–AGB stars. Star–forming regions are found at K−[12] > 9 (Fig. 10).
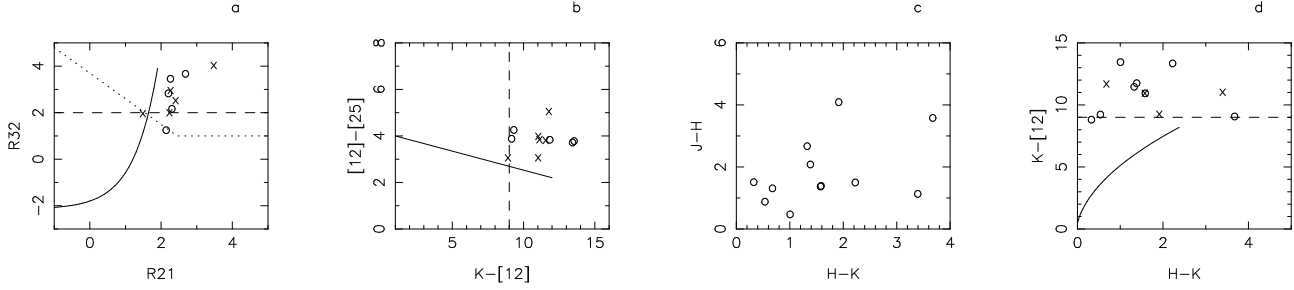
FIG. 10.— Two–colour diagrams for a sample of known OH–masing SFRs (Testi et al. 1998). Circles indicate reliable flux–density measurements and crosses colours from flux–density upper limits. In **a**, the IRAS two–colour diagram is plotted, showing the "OH–masing SFR" region (Section 5.3). In **b**, the near–mid–infrared diagram shows that SFRs all have K−[12] > 9 but are above the post–AGB line; compare to Fig. 8. Hence, the region 9<K−[12]<12 is shared by post–AGB stars and SFRs, but SFRs do not venture into the "PPN" region (Fig. 8b). In **c**, SFRs are seen to are spread over all NIR colours, hence a good fraction has H−K higher than post–AGB objects. In **d**, this means SFRs and post–AGB sources overlap only in the region K−[12] > 9 and H−K < 1.5.
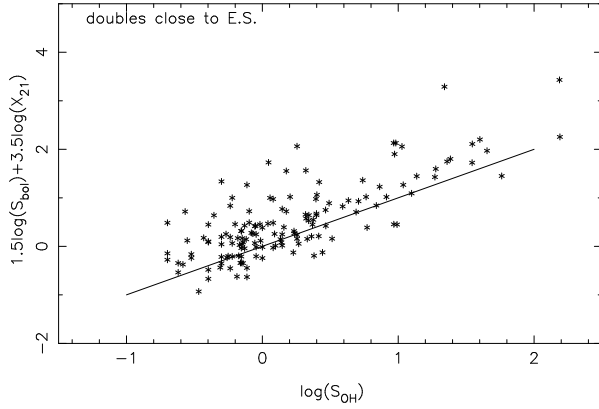

FIG. 11.— According to van der Veen (1989), the OH luminosity for objects along the evolutionary sequence is proportional to $L_*^2 X_{21}^6$, with $X_{21} \equiv S_{25}/S_{12}$. From this log–log plot, slightly different powers are found, 1.5 for the stellar luminosity and 3.5 for the flux–density ratio.
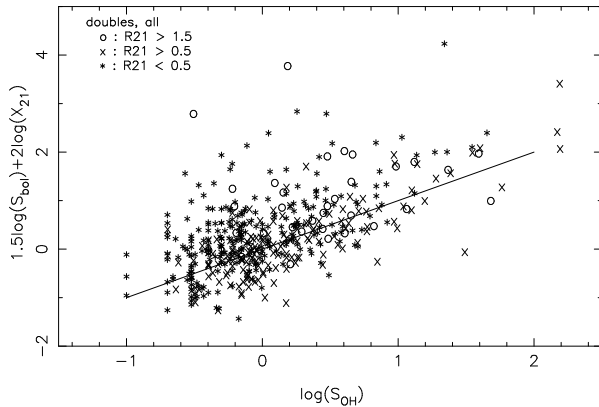

FIG. 12.— Same as Fig. 11, including (double–peaked) sources away from the evolutionary sequence. The power for X_{21} is 2 in this case.
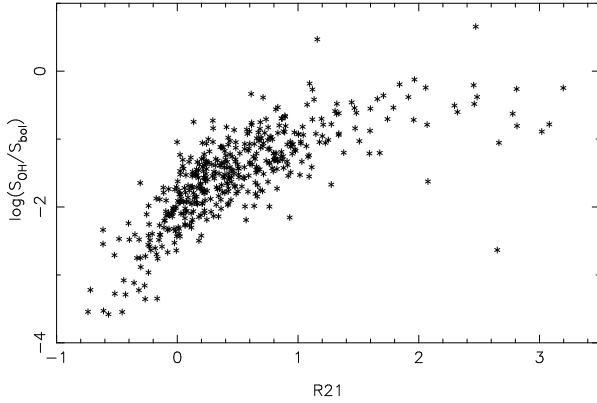
F$_{\rm IG}$. 13.— The maser "efficiency", $S_{\rm OH}/S_{\rm bol}$ (Section 6), is plotted logarithmically against IRAS colour R_{21}. For the bluest sources, it is $\propto X_{21}^6$, for the reddest sources $\propto X_{21}^0$ (both $S_{\rm OH}$ and $S_{\rm bol}$ are almost constant). Again, only double–peaked sources are plotted to avoid SFRs.

combination of the previous ones, but it can be used for sources with known K magnitude and no MSX or 60–μm association.

As seen in all the corresponding figures, the selection criteria, partly overlapping, are all entirely compatible, with just one or two sources breaking the rules.

Early post–AGB sources are selected by :

- (5) $[15-21] < 0.7$ and $[8-12] > 0.9$ (Fig. 3,4&8(a)), spectra in Fig. A4

- (6) $[12] - [25] > 4.164 - 0.164\,(K - [12])$ and K$-[12] > 9$ (Fig. 8a); these colours are shared by SFRs (Fig. 10)

Post–AGB sources in general, including the very earliest, may be selected by :

- (7) $(H-K) + 0.05 < 0.03\,((K-[12])+0.807)^2$, where early and late post–AGB objects can be distinguished by $[15 - 21]$ smaller or larger than 0.7 or even by $[8 - 12]$ smaller or larger than 0.9, respectively (Fig. 9, Fig. 3).

A group of blue possible post–AGB stars is found at :

- (8) $R_{32} > -0.2$ and $R_{21} > 0.2$, to the left of the evolutionary sequence ($R_{32} > -2.15 + 0.35\,\exp(1.5\,R_{21})$).

These are probably high–mass post–AGB sources (see Paper II)). Non–spherical–outflow objects (Fig. A7&6b) are likely to be found roughly in the region defined by Zijlstra et al. (2001).

5.2. Known PNe in the sample

Taking all the sources from our OH sample that are associated with a "Planetary Nebula" within 5″ according to SIMBAD, 10 out of 16 do satisfy the OH criteria of outflow velocity and flux density. Four of the 16 have a 2MASS association, with K$-[12] < 9.4$ and above the lines in Fig. 8&9.

Fourteen have an IRAS association, with 8 in the traditional PPN region to the right of the evolutionary sequence and 1 to the left, with $V_{\rm exp} > 15$ km s^{-1} and very blue MSX colours. Of the 12, out of 16, sources with MSX association, 5 are in the first quadrant (Fig. 3).

Spectra of all 16 sources are given in Fig. A6. Even of this group of selected "Planetary Nebulae", 75% have regular, double–peaked spectra. Even two known "bipolar planetary nebulae" are in this group of 16 : OH353.844+02.984 (Fig. A6(3); Kwok et al. 1996) and OH348.813−02.840 (Fig. A6(6); Hrivnak et al. 1999). The latter satisfies all our selection criteria for which its properties are known, including slow, regular outflow.

In summary, sources classified as "planetary nebulae" in fact cover a range of post–AGB evolutionary stages. As we noted in the caption of Fig. 7, a source that still harbours 1612–MHz emission is unlikely to be a full–blown PN. It would be good practice to name such objects PPN or OHPN (see Introduction).

5.3. Colours of SFR sources

It is hard to define clear–cut selection criteria to find SFRs in an OH sample, especially to tell them apart from PPN. A sample of known OH–masing SFRs with NIR data, from the literature (Testi et al. 1998), is used to check their infrared behaviour with respect to post–AGB stars. In Fig. 10, several two–colour diagrams are given for comparison with the diagrams in the rest of the paper. The dotted line in Fig. 10(a) outlines the OH–masing SFR region, slightly adapted from Braz & Sivagnanam (1987), who claim that non–OH–masing SFRs are found to the left of this region, at lower R_{21} but similar R_{32}.

Interestingly, in K$-[12]$ versus $[12]-[25]$ (Fig. 10b), the SFRs lie above the empirical line drawn in Fig. 8, but at higher K$-[12]$ than the PPN sources. The selected sources in Fig. 8b and the SFRs in Fig. 10b are perfectly separated, although there are some earlier post–AGB sources in the region K$-[12] > 9$ (Fig. 8a). In Fig. 10d, the SFRs are also in the post–AGB region, again at higher K$-[12]$ and mostly higher H$-$K (Fig. 10c). Three SFRS with a reliable MSX identification with (some) well–determined flux densities are all in quadrant II.

TABLE 1

FRACTIONS (IN %) OF DOUBLE (D), SINGLE (S) AND IRREGULAR (I) SPECTRA FOR SEVERAL POST–AGB SELECTIONS PLUS COMPARISON PN AND AGB SAMPLES (JUDGED BY EYE FROM THE FIGURES IN APPENDIX A). THE FIRST FOUR ROWS CORRESPOND TO SELECTIONS 1,8,2 AND 5 IN SECTION 5.1, RESPECTIVELY

	D	S	I	comment
Right	75	10	15	iras (low–mass)
Left	65	7	28	iras (high–mass)
Q1	61	17	22	msx (old)
Q4	75	0	25	msx (young)
PN	75	10	15	simbad (Section 5.2)
AGB	80	5	15	iras (on evol. seq.)
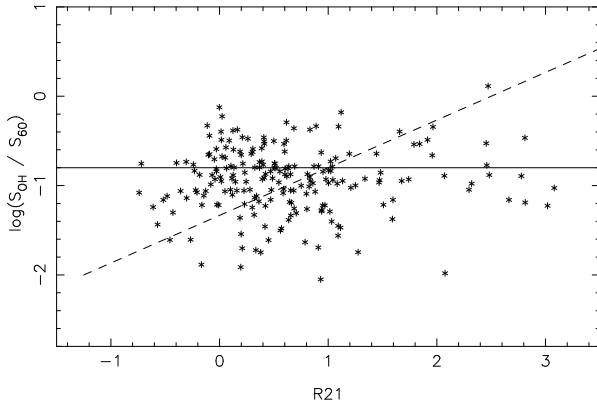
FIG. 14.— The ratio of OH–peak flux density and 60–μm flux density plotted logarithmically against IRAS colour R_{21} for all double–peaked sources. Of all IRAS flux densities, S_{60} correlates most strongly, almost linearly, with S_{OH}. The S_{60} contains the 53–μm pumping line. The dashed line is the relation found by Chen et al. (2001) for S_{OH}/S_{35}, with S_{35} the interpolated flux density at the 35–μm pumping line.

6. MASER–INFRARED CORRELATION

In order to determine a maser "efficiency" in terms of OH flux density as a function of stellar flux, we derive the bolometric flux, $S_{\text{bol}} \equiv S_{12} * BC_{12}$, using the bolometric correction

$$BC_{12} = 0.7 + 2.9 \exp(-3.0\,R_{21}) + 0.9 \exp(0.7\,R_{21}) \quad (2)$$

from van der Veen & Breukers (1989). If all the stellar light is recycled in the infrared, then $S_* \equiv S_{\text{bol}}$. Van der Veen (1989) gives, for sources on the evolutionary sequence, $S_{\text{OH}} = S_*^2 X_{21}^6$, where $X_{21} \equiv S_{25}/S_{12}$. We find that this relation is not exactly right and also that the scatter around it is very large. Rather, for sources close to the evolutionary sequence (Fig. 11),

$$S_{\text{OH}} = S_{\text{bol}}^{1.5} X_{21}^{3.5} \qquad (3a)$$

and for the whole sample in general (Fig. 12)

$$S_{\text{OH}} = S_{\text{bol}}^{1.5} X_{21}^{2}. \qquad (3b)$$

However, the "maser efficiency", defined as $S_{\text{OH}}/S_{\text{bol}}$, is proportional to X_{21}^6 for the very bluest sources (Fig. 13), since of course S_{bol} itself varies strongly with X_{21} (Equation 2). For the reddest sources, the maser efficiency is virtually constant. With a scatter of about a decade in these log–log plots these relations cannot be used on a one–by–one basis. We can conclude, however, that statistically the OH flux density of circumstellar masers is a well–behaved function of "pumping" (S_{bol}) and "optical depth" (R_{21}).

Moreover, there is a very clear, almost linear correlation between the 60–μm flux density and the OH flux density (Fig. 14). The 60–μm band contains the 53–μm pumping line, which may explain the correlation with "available pumping photons", even though the line would be too narrow to influence the wide–band flux. The red post–AGB sources have surprisingly similar flux–density ratio to the evolutionary–sequence sources. In Fig. 14, we plot the slope of the relation found by Chen et al. (2001) for the ratio S_{OH}/S_{35}, with the IRAS flux density at the main pumping line at 35 μm derived by interpolation. Not only is their relation not linear, it is also less tight, so it seems the S_{60} is a more uniform indicator of pumping than the interpolated S_{35}, possibly due to contaminating lines in the S_{25} band.

7. CONCLUSIONS

An extensive comparison is given between several infrared and OH–maser properties of an OH–selected sample of objects in the galactic plane. All the OH specifics in this paper apply only to the 1612–MHz maser line and may be (quite) different when studying the main lines. Four different selection criteria are presented for finding red proto–planetary nebulae with OH masers, that all give consistent selections. Most efficient in separating post–AGB stars is the MSX two–colour diagram for $[8 - 12]$ and $[15 - 21]$ that splits into four clear quadrants, containing primarily PPNe, SFRs, AGB objects and post–AGB stars, respectively. Two selection criteria are presented for finding early post–AGB OH stars and one for post–AGB stars of all ages. A significant group of blue (likely) post–AGB stars with 60–μm excess remains unselected by all of the above criteria; these will be discussed in Paper II.

None of the selected post–AGB groups show any true prevalence of irregular or extreme–velocity outflows, rather about 70% of their OH spectra are typical of regular, spherical, thin–shell outflow with velocities between 9 km s^{-1} and 15 km s^{-1}. However, the sources with very irregular spectra are located roughly in the bipolar–outflow IRAS region defined by Zijlstra et al. (2001). The reddest PPN may have a slightly higher fraction of genuine single–peaked sources.

Maser efficiency, defined as the ratio of OH luminosity to bolometric luminosity, increases steeply with IRAS colour R_{21} for blue sources, but is almost constant for the reddest sources. Of all IRAS flux densities, the OH maser correlates most strongly, and linearly, with the 60–μm flux density.

REFERENCES

Bedijn P., 1987, A&A, 186, 136
Braz M., Sivagnanam P., 1987, A&A, 181, 19
Chen P., Szczerba R., Kwok S., Volk K., 2001, A&A, 368, 1006
Garcia–Lario P., Manchado A., Pych W., Pottasch S., 1997, A&AS, 126, 479
Habing H., Tignon J., Tielens A., 1994, A&A, 286, 523
Hrivnak B., Kwok S, Su K., 1999, ApJ, 524, 849
Kwok S., Hrivnak B., Zhang C., Langill P., 1996, ApJ, 472, 287
Lewis B., 1989, ApJ, 338, 234
Lewis B., 1994, ApJS, 93, 549
Likkel L., 1989, ApJ, 344, 350
Oudmaijer R., van der Veen W., Waters L., Trams N., Waelkens C., Engelsman E., 1992, A&AS, 96, 625
Sevenster M., Chapman J., Habing H., Killeen N., Lindqvist M., 1997a, A&AS, 122, 79
Sevenster M., Chapman J., Habing H., Killeen N., Lindqvist M., 1997b, A&AS, 124, 509

Sevenster M.N, 2002, AJ, 00, 000 (Paper II)
Sevenster M., van Langevelde H., Moody R., Chapman J., Habing H., Killeen N., 2001, A&A, 366, 481
Te Lintel Hekkert P., Habing H., Caswell J., Norris R., Haynes R., 1991, A&AS, 90, 327
Te Lintel Hekkert P., Chapman J., 1996, A&AS, 119, 459
Testi L., Felli M., Persi P., Roth M., 1998, A&AS, 129, 495
van der Veen W., 1989, A&A, 210, 127
van der Veen W., Breukers R., 1989, A&A, 213, 133
van der Veen W., Habing H., 1988, A&A, 194, 125
van Hoof P., Oudmaijer R., Waters L., 1997, MNRAS, 289, 371
van Loon J., Zijlstra A., Whitelock P., Te Lintel Hekkert P., Chapman J., et al. 1998, A&A, 329, 169
Zijlstra A., Te Lintel Hekkert P., Pottasch S., Caswell J., Ratag M., Habing H., 1989, A&A, 217, 157
Zijlstra A., Chapman J., Te Lintel Hekkert P., Likkel L., Comeron F., et al. 2001, MNRAS, 322, 280
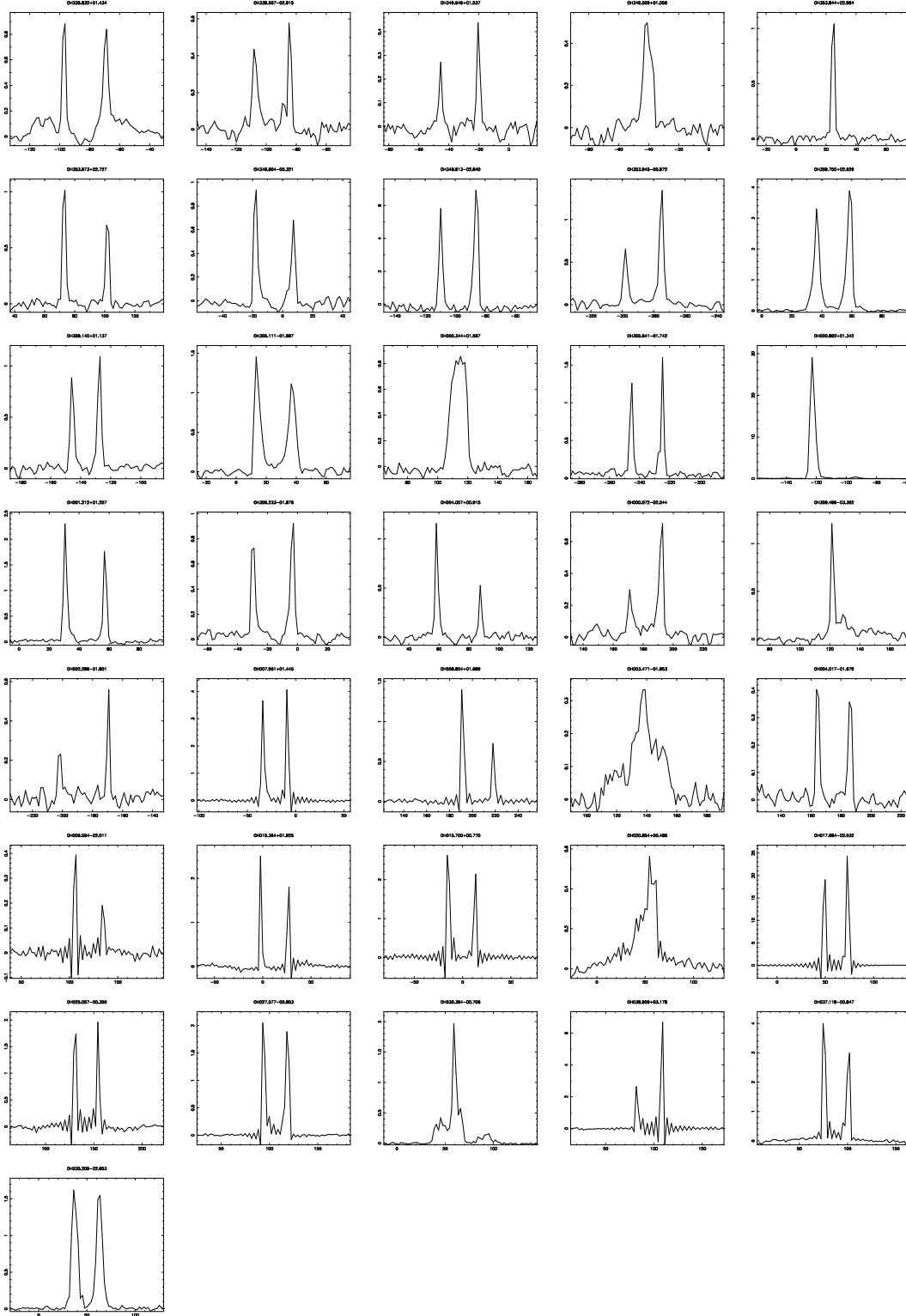
APPENDIX

SPECTRA

FIG. A1.— All sources with $R_{32} < 1.5$ and $R_{21} > 1.4$ (item 1 in Section 5.1). Note that all spectra in this appendix have flux densities that are NOT corrected for primary–beam dilution. In the text, quoted flux densities ARE corrected.
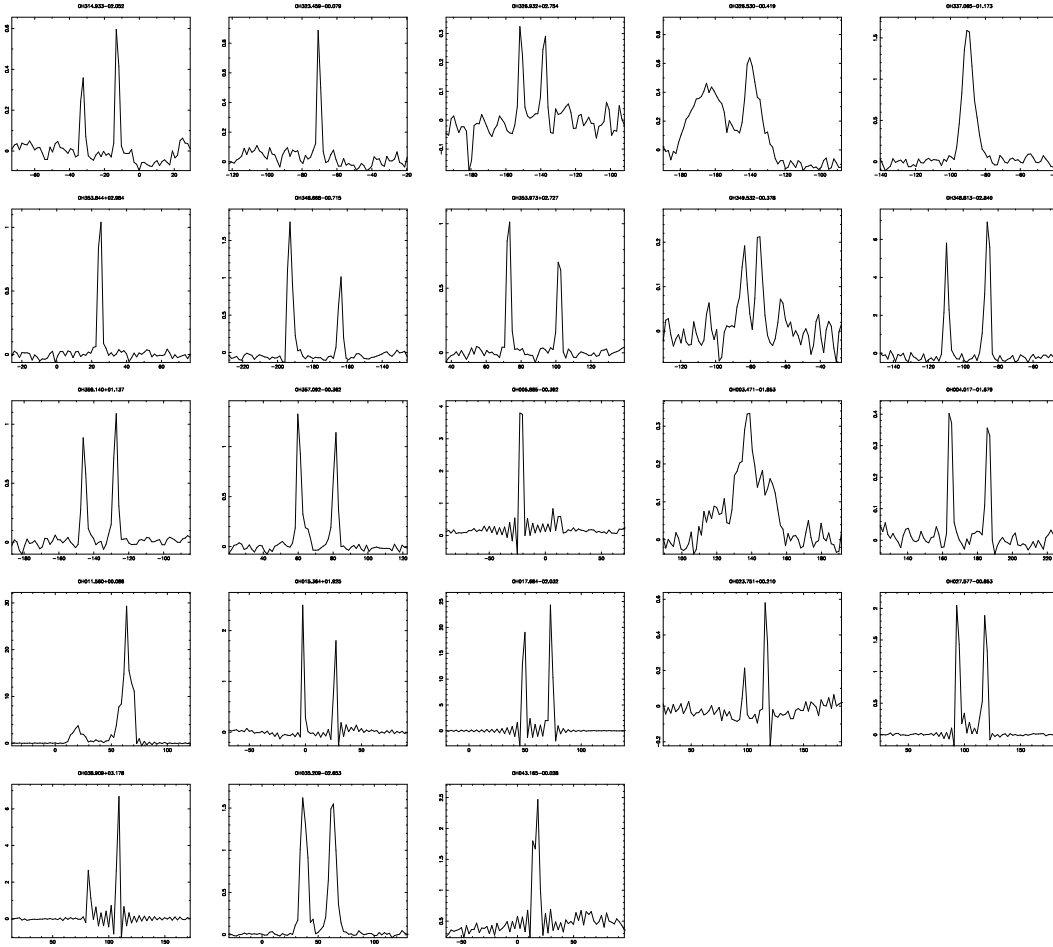
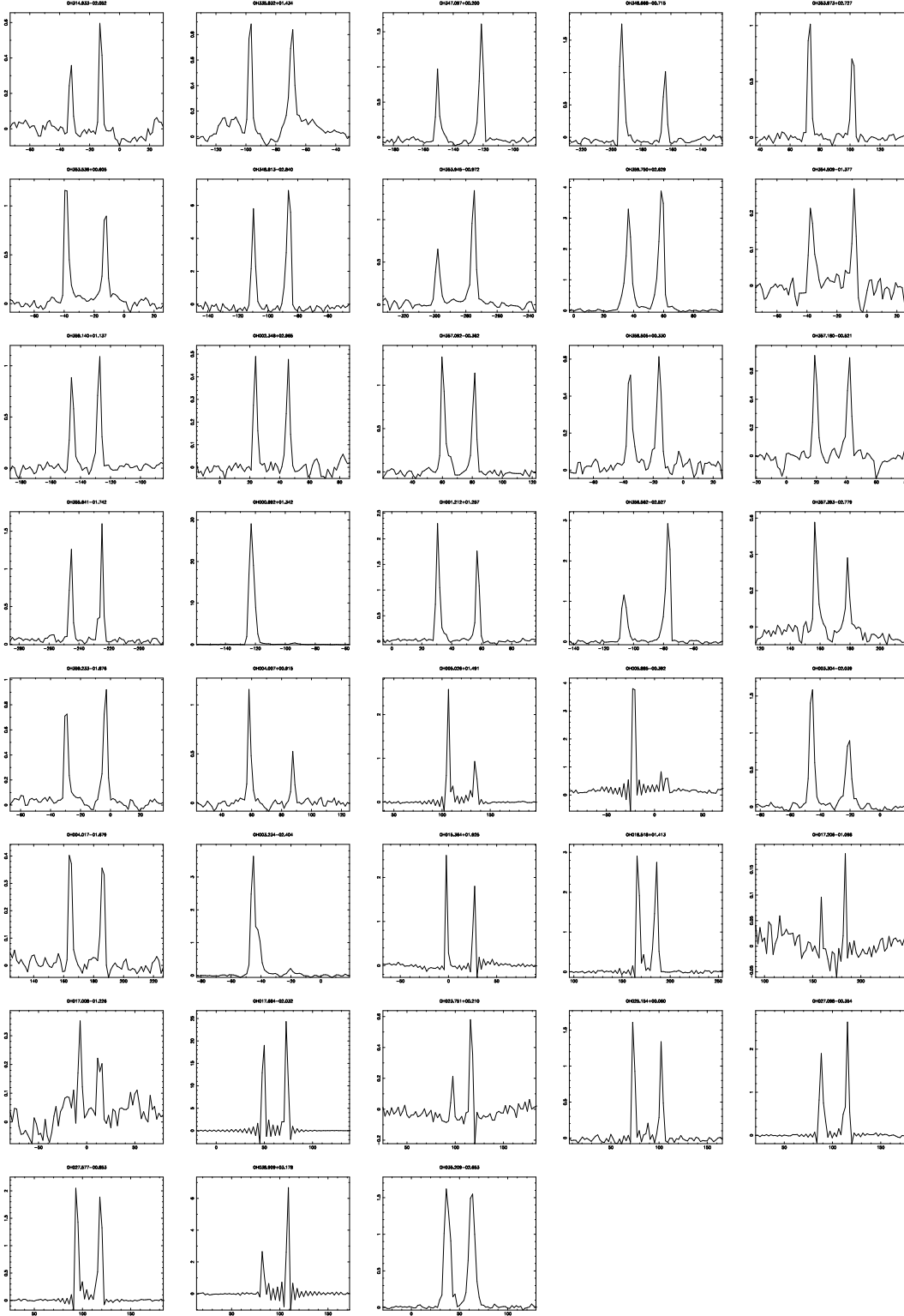FIG. A2.—   All sources with [8-12]> 0.9 and [15-21]>0.7 (item 2 in Section 5.1).

FIG. A3.— All sources with [15-21]>0.7 and $9\,\mathrm{km\,s^{-1}}\,V<15\ \mathrm{km\,s^{-1}}$ and sum of the blue– and red–shifted OH peak flux densities larger than 1 Jy (item 3 in Section 5.1, Fig. 8). This gives [12]-[25]>3 and [8-12]>0.9 .
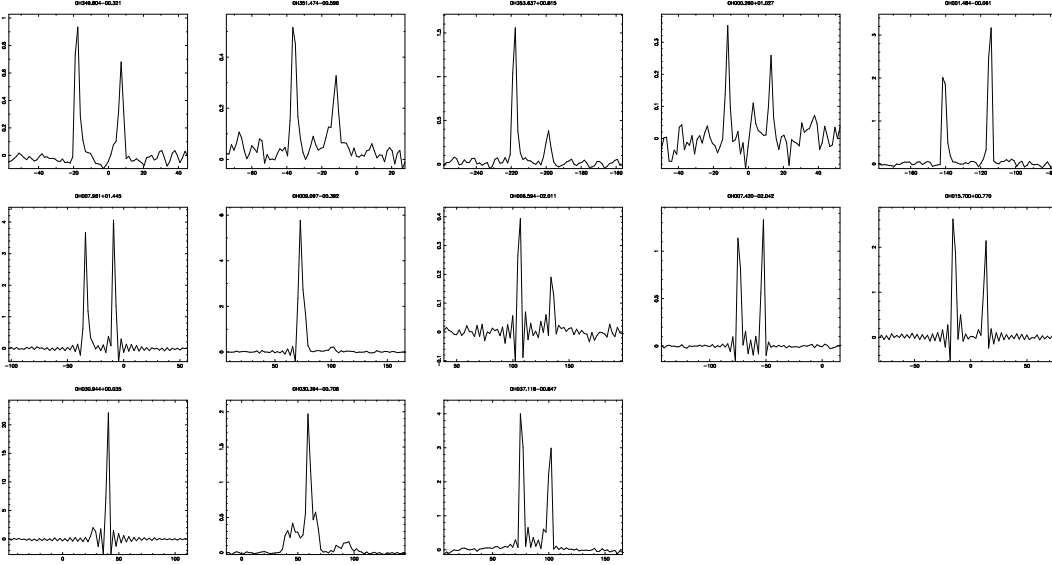
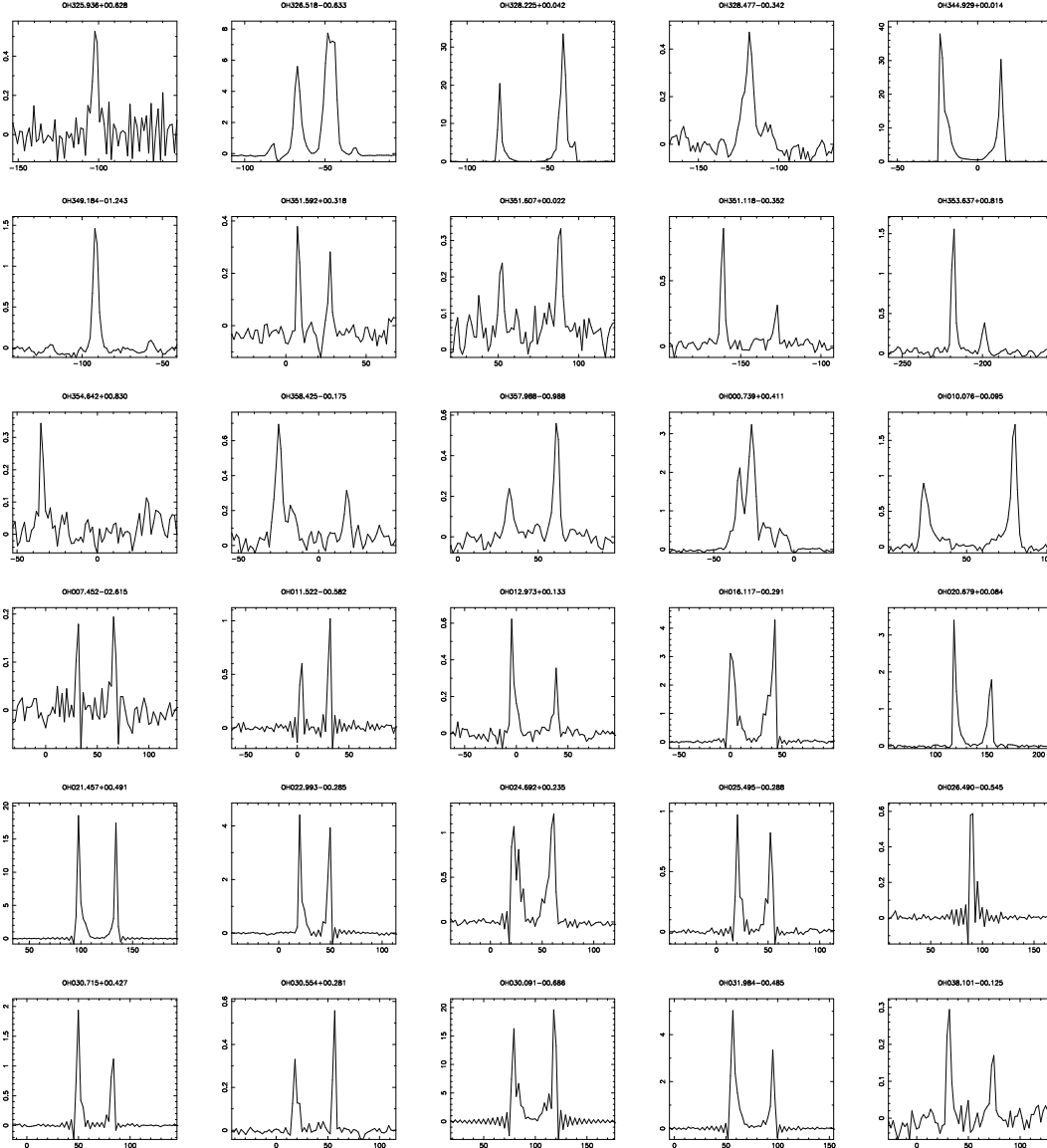FIG. A4.— Sources with [15-21]<0.7 and [8-12]>0.9 (item 5 in Section 5.1). Second last source has [15-21]∼0.7 though

FIG. A5.— All sources with $R_{32} > -0.2$ and $R_{21} > 0.2$ to the left of the evolutionary sequence in the IRAS two–colour diagram (item 8 in Section 5.1, Fig. 4).
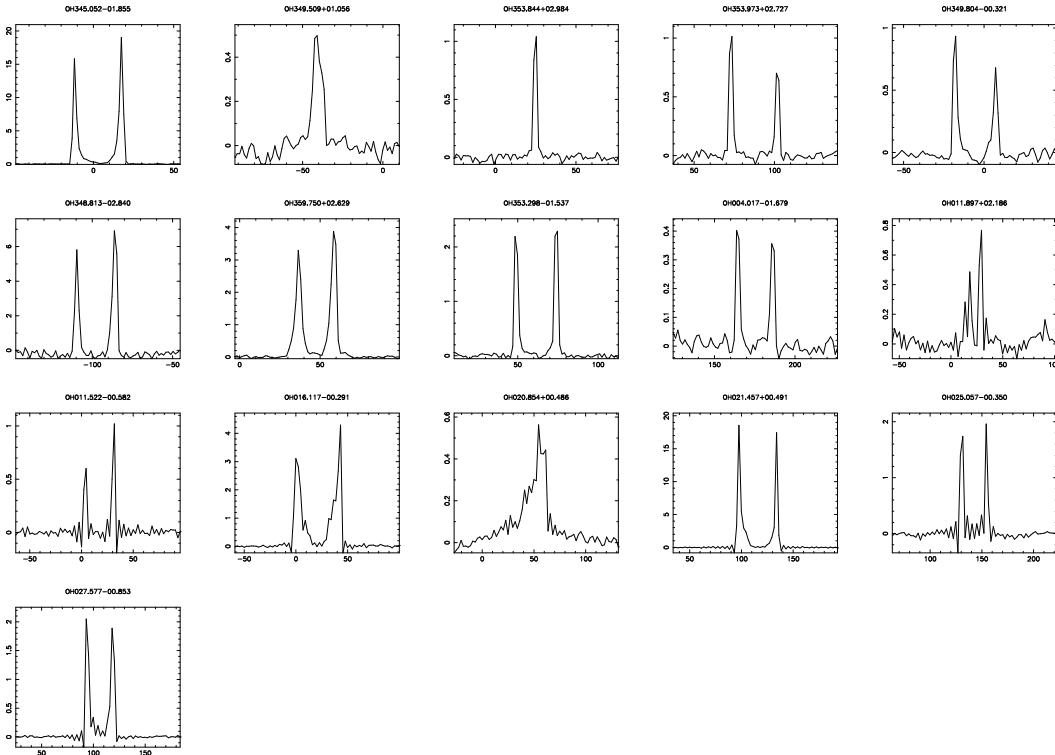
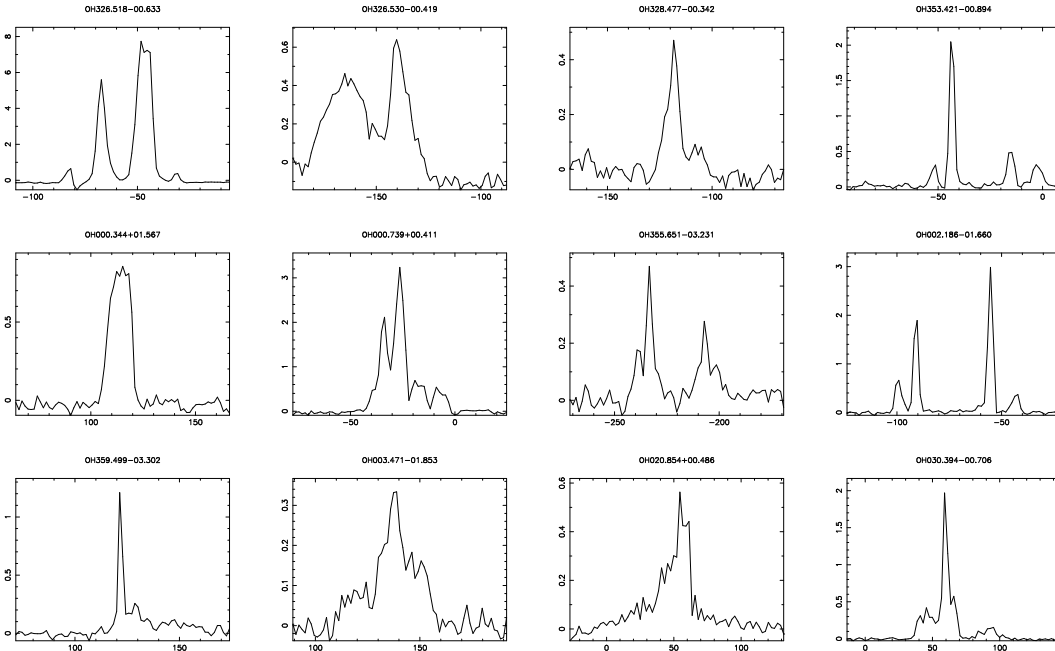FIG. A6.— All sources with a SIMBAD association of PN within 5″ (Section 5.2).

FIG. A7.— All sources with "irregular spectra", defined by $w_{20} \gg \Delta V$ (Section 3).
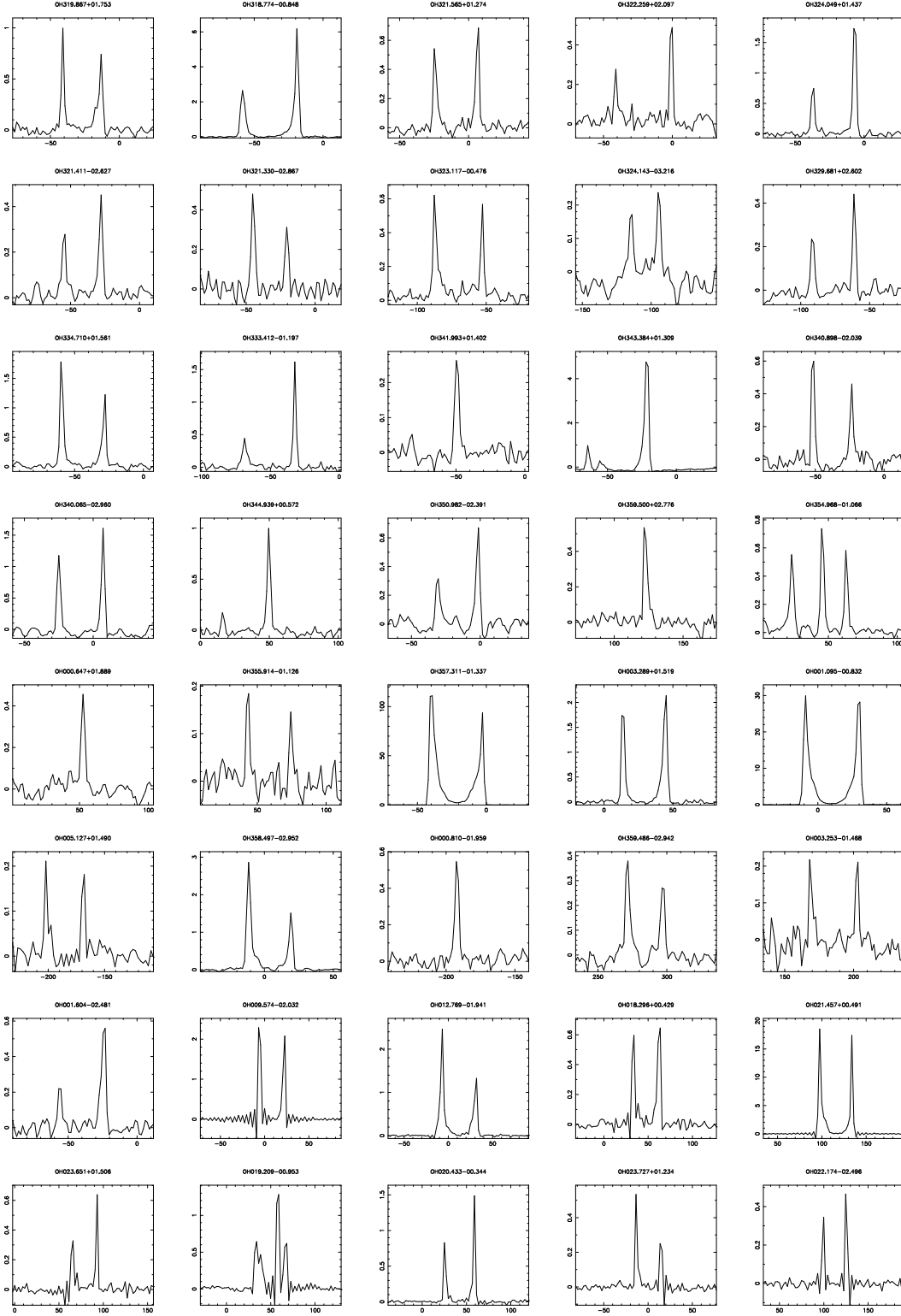
FIG. A8.— Thermally–pulsing AGB sources, on the IRAS evolutionary sequence (solid curve in Fig. 4).